Article

Microstructure and Mechanical Properties at Elevated Temperature of Powder Metallurgy Al-Zn-Mg-Cu Alloy Subjected to Hot Extrusion

Weihao Han [1], Yang Li [1], Pei Li [1], Guoping Su [1,2], Chenzeng Zhang [1], Chunfang Sun [1], Cunguang Chen [1,3,*], Fang Yang [1,*] and Zhimeng Guo [1]

1   Institute for Advanced Materials and Technology, University of Science and Technology Beijing, Beijing 100083, China; b20160508@xs.ustb.edu.cn (W.H.); g20209386@xs.ustb.edu.cn (Y.L.); b20160553@xs.ustb.edu.cn (P.L.); D202110646@xs.ustb.edu.cn (G.S.); b20190571@xs.ustb.edu.cn (C.Z.); sunchunfang2020@163.com (C.S.); zmguo@ustb.edu.cn (Z.G.)
2   AlTi New Materials (Xiang He) Co., Ltd., Langfang 065400, China
3   State Key Laboratory for Advanced Metals and Materials, University of Science and Technology Beijing, Beijing 100083, China
*   Correspondence: cgchen@ustb.edu.cn (C.C.); yangfang@ustb.edu.cn (F.Y.)

Abstract: In this work, Al-Zn-Mg-Cu powders containing 0.15 and 0.33 wt % oxygen were utilized to prepare high-strength aluminum alloys through the process of cold isostatic pressing, sintering, hot extrusion, and heat treatment. Microstructural and mechanical properties at elevated temperatures of 250, 350, and 450 °C were investigated by scanning electron microscopy (SEM), electron backscatter diffraction (EBSD), transmission electron microscopy (TEM), and high-temperature tensile tests. Results showed that the tensile strengths of the obtained Al-Zn-Mg-Cu alloys with 0.15 wt % oxygen were 185, 46, and 18 MPa at 250, 350, and 450 °C, respectively. When the oxygen content of Al-Zn-Mg-Cu alloy rose to 0.33 wt %, the tensile strengths at the corresponding temperature reached up to 205, 68, and 25 MPa, respectively. The excellent high-temperature performance could be attributed to double hindrance to dislocation motion and grain boundary migration by a large amount of nano γ-Al_2O_3 created by the in-creased oxygen, thereby resulting in fine grains even at high temperatures.

Keywords: powder metallurgy; Al-Zn-Mg-Cu alloy; high temperature strength; oxygen content

1. Introduction

Al-Zn-Mg-Cu alloys are widely used in aircraft, armor, and military applications due to their high modulus, low density, and excellent stress corrosion resistance [1–5]. In harsh application places, certain requirements are put forward for the heat resistance of Al-Zn-Mg-Cu alloys [6]. For instance, current oil drill pipes are usually exposed to high temperatures (less than 200 °C) and high pressure (the formation pressure of a 4000 m oil well is about 50–60 Mpa). With the depletion of shallow well oil resources, the trend of future oil exploration is gradually developing towards deep well drilling and offshore drilling, which puts forward higher requirements for drilling and production tools [7–10]. Al-Zn-Mg-Cu alloys are often used as a structural fuselage component during service at slightly elevated temperatures (83–177 °C) for a short period of time [11,12]. Therefore, it is necessary to improving the high-temperature strength of Al-Zn-Mg-Cu alloys. The most effective way to improve Al-Zn-Mg-Cu alloys is to introduce a thermodynamically stable second phase [13].

Currently, adding Zr and Sc to Al-Zn-Mg-Cu alloys to form thermally stable Al_3(Zr, Sc) dispersed in the matrix to improve its room-temperature and high-temperature performance is mainstream research [14–17]. Martin et al. [18] found that increasing the Zr content resulted in higher hardness of the alloy after heat treatment. This phenomenon was mainly due to the exceptionally high thermal stability provided by the presence of

large Al_3Zr precipitates (100–500 nm) at the GBs, i.e., which improves the recrystallization resistance during solution treatment. Ying et al. [19] studied the effect of 0.4 wt % Sc on the hot deformation processing of Al-Zn-Mg-Cu alloy, and found that a remarkable grain refinement and retardation of recrystallization had occurred during hot extrusion, which can be attributed to the pinning effect on the dislocation movement and grain boundary migration in Sc-containing alloys. However, Zr and Sc are quite expensive [19]. Thus, this adds higher costs in the production process.

Along the line of introducing a second phase with excellent thermal stability, powder metallurgy (PM) aluminum alloys have natural advantages. Previous studies [20–22] showed that there is a nanoscale Al_2O_3 film on the surface of aluminum powder. Al_2O_3 films can be broken during the sintering and deformation process, and thus play a role in pinning the grain boundaries and dislocations. Therefore, PM Al has excellent thermal stability [23,24]. Nosko et al. [25] used pure aluminum powders with different particle sizes for sintering and extrusion experiments, and found that, as the powder particle size decreased, the content of alumina gradually increased, thereby inhibiting the occurrence of recrystallization, and bringing higher alloy strength and hardness. Our previous research [23] on the thermal stability of powder metallurgy pure aluminum also confirmed this result. However, there are few studies focusing on the high-temperature performance of PM Al-Zn-Mg-Cu alloys.

In this work, the high-temperature tensile properties of powder metallurgy Al-Zn-Mg-Cu alloys with different oxygen contents were studied, and the microstructure and tensile fracture morphology at high temperature were analyzed.

2. Experimental Procedure

Al-Zn-Mg-Cu alloys with different oxygen contents were manufactured by the powder metallurgy method. The major alloying elements of Al-Zn-Mg-Cu alloys are shown in Table 1. The composition was close to that of the AA7055 aluminum alloy without the Zr element. Al alloy powders with oxygen content of 0.15 wt % were obtained by V-type blending for 5 h, and powders with oxygen content of 0.33 wt % were obtained by a drum ball mill with a ball-to-material ratio of 9:1 for 5 h. Compared with blending, the increase in oxygen content by ball milling was mainly due to the generation of continuous oxidation film on new powder surfaces. The two alloys were marked as blending (BL) and ball milling (BM), respectively. All powders were compacted under pressure of 180 Mpa for 2 min in a rubber mold by cold isostatic press. The green compact was sintered in vacuum at 580 °C for 2 h to obtain Al-Zn-Mg-Cu alloy ingots with a thickness of 24 mm and a width of 135 mm. Hot extrusion was carried out at 420 °C with an extrusion speed of 0.5 mm/s and an extrusion ratio of 9:1. Then, solution treatment and aging treatment were carried out at 470 °C/2 h and 120 °C/24 h. According to ASTM E21-13, tensile tests were carried out at 25, 250, 350, and 450 °C with a deformation rate of 0.05 mm/s, a heating rate of 15 °C/min, and a holding time of 15 min. To ensure accuracy, each experiment was performed for three times.

Table 1. Composition of Al-Zn-Mg-Cu alloys in this work and AA7055 alloy.

Sample	Zn	Mg	Cu	Zr	Al
Nominal alloy	8.3	2.3	2.5	-	Bal.
As-sintered BL alloy	8.16	2.28	2.48	-	Bal.
As-sintered BM alloy	8.12	2.27	2.49	-	Bal.
AA7055	7.6~8.4	1.8~2.3	2.0~2.6	0.08~0.25	Bal.

The oxygen content of the two kinds of Al-Zn-Mg-Cu alloy powders were tested by an ONH analyzer (LECO-ONH836, LECO Inc., San Jose, CA, USA) with 5700 W power. BL and BM alloying element content was determined by Inductively coupled plasma mass spectrometry (ICP-MS, Agilent 5110, Agilent Inc., Palo Alto, CA, USA), according to ASTM E3061-17. SEM samples were taken from the clamping end of the tensile specimen. Samples

were prepared by grinding with SiC paper up to 5000 grit and mechanically polishing them on a running disc at 400 rpm with a 0.25 μm diamond polishing paste. Changes in the second phases at different temperatures were observed by field emission scanning electron microscope (FESEM, SUPRATM 55, Carl-Zeiss Inc., Oberkochen, GER) with an operating condition of 15 kV. EBSD was performed to analyze the crystallographic information. EBSD samples were the same as the SEM samples, but eventually electrochemically polished in 10% perchloric acid alcohol solution at voltage of 15 V for 30 s at room temperature. EBSD analysis was carried out at 20 kV by using a Carl-Zeiss SUPRA 55 equipped with an electron backscatter diffraction detector (Oxford Nordlys Nano, Oxford Instrument Inc., Oxfrod, UK). TEM samples were cut from the cross-section of the as-heat-treated BM alloy, ground to a thickness of 0.05 mm, and then twin-jet electropolished using a solution of 20 vol % perchloric acid and 80 vol % methanol. A transmission electron microscope (TEM, Tecnai G2 F30, Thermo Fisher Scientific Inc., Waltham, MA, USA) was used to observe the distribution of oxides with an operating condition of 200 kV.

3. Results and Discussion

Figure 1a,b show the grain orientation images (OIM) of BL and BM alloys after heat treatment. Even after high-temperature solution treatment at 470 °C/2 h, the grain size of BL alloys remained fine, and the average grain size was 5.15 μm. The BM alloy had finer grains with an average grain size of 3.16 μm. More Al_2O_3 particles were formed after the ball-milling and oxygenation process, thereby inhibiting the recrystallization during thermal deformation processing and heat treatment. Figure 1c,d show SEM pictures of BL and BM alloys after heat treatment. There was only a small amount of second phase (white particles) in the matrix after heat treatment. This is because, after the solution treatment, a large amount of $MgZn_2$ and other second phases was supersaturated and dissolved into the matrix [26]. After T6 aging treatment, nanoscale second phases were formed that were difficult to observe in SEM.
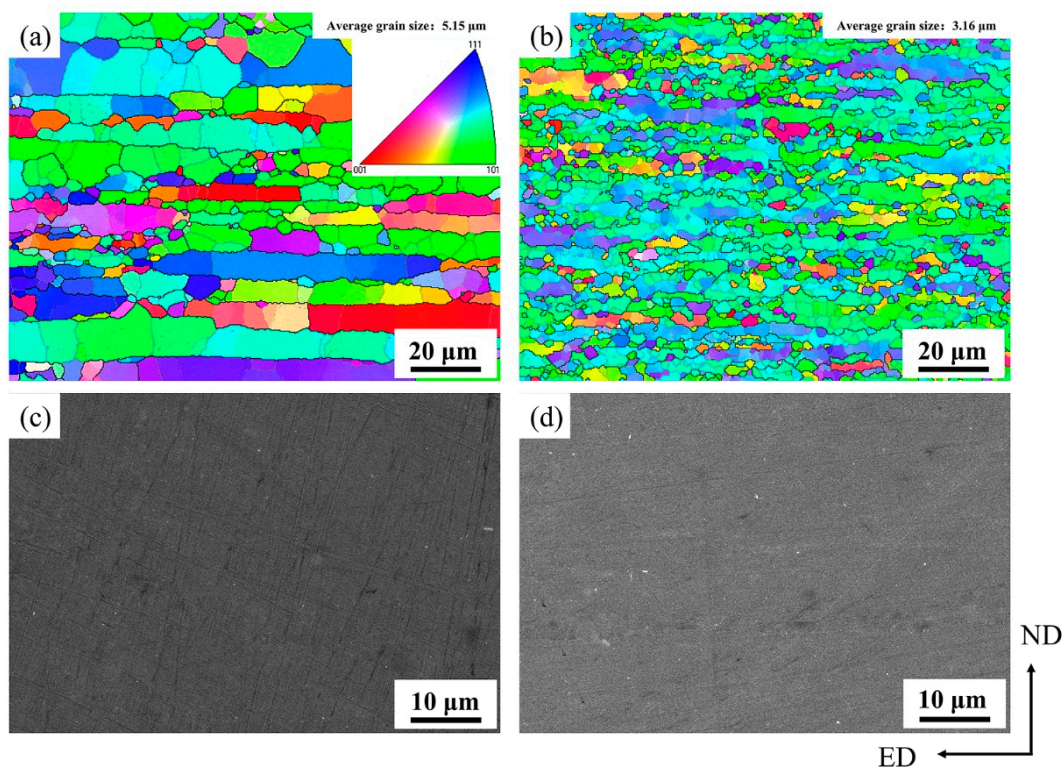

Figure 1. Grain orientation maps and SEM images of as-heat-treated (**a**,**c**) BL alloy and (**b**,**d**) BM alloy. (ED, extrusion direction; ND and TD, thickness and width direction of the sheet, respectively).

Figure 2 shows the pole figure (PF) of the BL and BM alloys in the heat-treated state. The BL alloy had three recrystallized textures: {001} <001>, {001} <111> and {011} <111>, with a texture strength of 12.92. The main texture of BM alloy is {111} <112>, and the texture strength reaches 19.33.
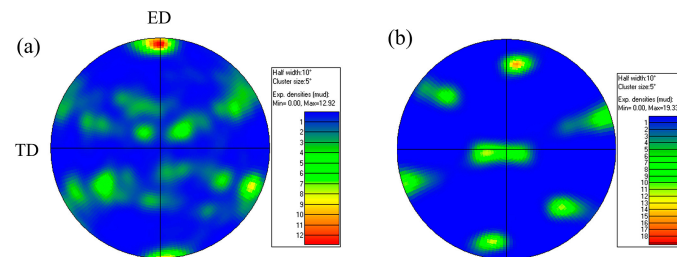

Figure 2. (111) Pole figures of (**a**) BL alloy and (**b**) BM alloy after heat treatment.

Figure 3a shows TEM micrographs of the BM alloy, which consisted of a large number of black particles (less than 100 nm) with dislocation tangles. Part of the dislocation tangles were packed at the black particles. Figure 3b shows the calibration of the diffraction pattern. Figure 3b shows that the black phase was γ-Al$_2$O$_3$, which is consistent with previous studies [27].
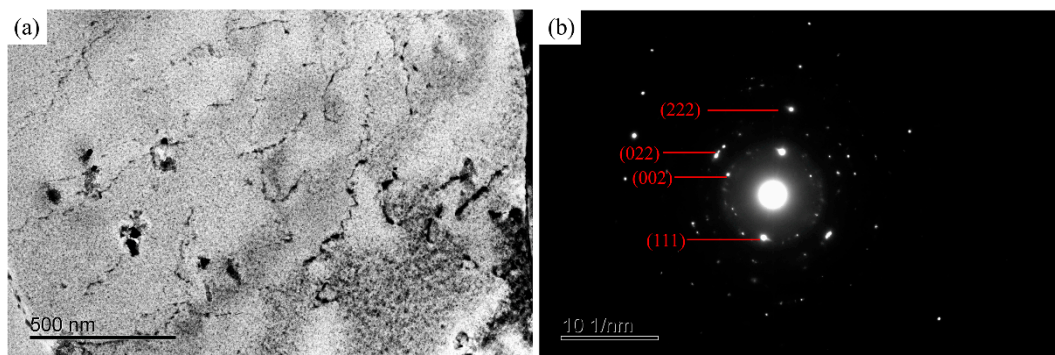

Figure 3. (**a**) TEM photographs of γ-Al$_2$O$_3$ dispersoids; (**b**) corresponding selected area electron diffraction (SAED).

Figure 4a–c show the OIM of the tensile BL samples at 250, 350, and 450 °C. The grains sizes of the samples were 5.37, 5.89, and 6.27 μm at 250, 350, and 450 °C, respectively. Grain size increased by 4.3%, 14.4%, and 21.7%, respectively. The grain sizes of the BM samples were 3.22, 3.32, and 3.43 μm at 250, 350, and 450 °C, respectively. The large crystal grains were still lath. As the temperature rose, some of the internal subcrystals merged. The grain size of the BM alloy was maintained at a small scale. Therefore, the BM alloy achieved a finer microstructure compared with the BL alloy due to the higher oxygen content.

Figure 5 shows the pole figure (PF) of BL and BM alloys. The textures of the BL and BM alloys at 250, 350, and 450 °C were unchanged. The BL alloy had three textures: {001} <001>, {001} <111>, and {011} <111>, and the BM alloy had one texture: {111} <112>. The texture strength of both alloys gradually decreased with temperature increasing.

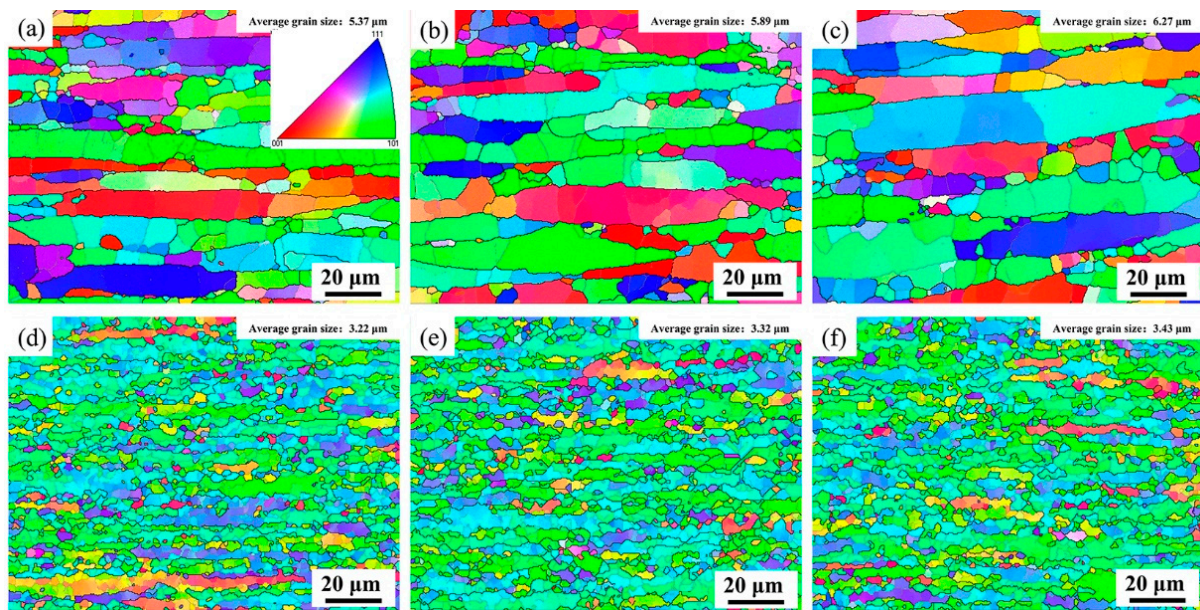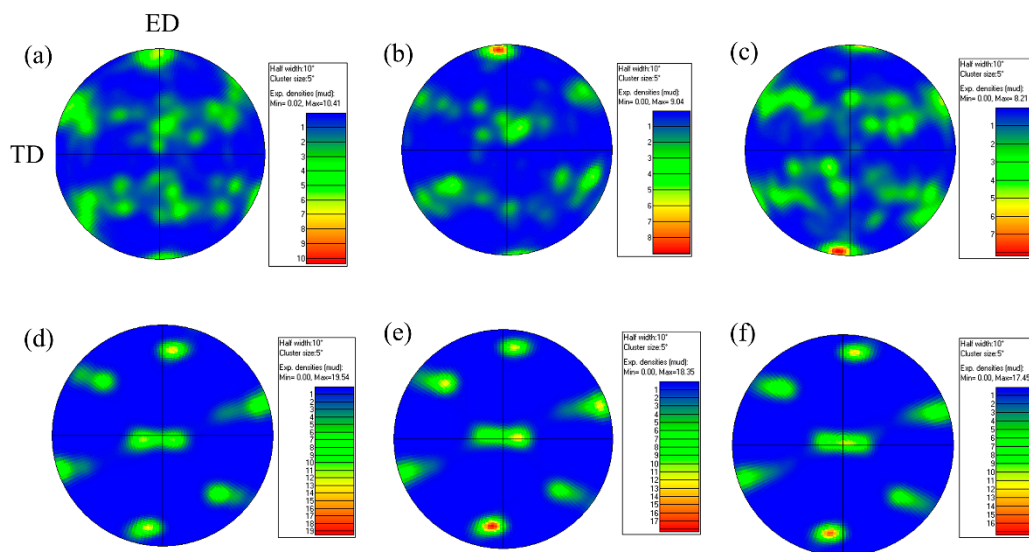**Figure 4.** Grain orientation maps of BL alloys at (**a**) 250 °C, (**b**) 350 °C, (**c**) 450 °C, and BM alloys at (**d**) 250 °C, (**e**) 350 °C, (**f**) 450 °C.

Figure 5. (111) Pole figures of BL alloy at (**a**) 250 °C, (**b**) 350 °C, (**c**) 450 °C, and BM alloy at (**d**) 250 °C, (**e**) 350 °C, (**f**) 450 °C.

Figure 6 is SEM images magnified 5000 times. There was no obvious second-phase growth phenomenon in either alloy at 250 °C. The second phase appeared at 350 °C, and the number of the second phase increased significantly at 450 °C. The reason for this phenomenon is the precipitation sequence of Al-Zn-Mg-Cu (α-supersaturated solid solution → GP (I, II) zones→ η' phase → η ($MgZn_2$) phase) [28]. The transition from the η' phase to the η ($MgZn_2$) phase had occurred at 250 °C, and the η ($MgZn_2$) phase was still on a small scale at this time. The second phase gradually grew at 350 °C. Although 450 °C was close to the solid solution temperature, the second phase was still relatively coarse when the holding time was 15 min and did not reach the equilibrium state. Comparing the second phases of the BL and BM alloys shows the second phases in BM alloys were denser. This is because the η ($MgZn_2$) phase was mainly precipitated along the grain boundary and the BM alloy has finer grains. Combined with TEM observation, the phase formed by the oxide was γ- Al_2O_3. Since γ-Al_2O_3 was very stable at the temperature of processing and

heat treatment in this paper, it was difficult to react with other elements. Phase reactions during high-temperature stretching can be analyzed as conventional Al-Zn-Mg-Cu, which has been carried out in numerous studies.
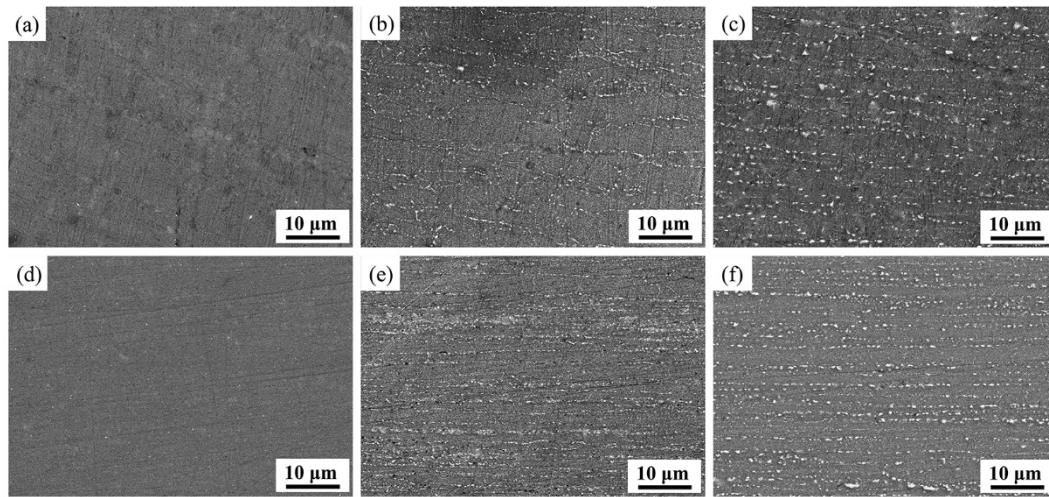

Figure 6. SEM images of BL alloy: (**a**) 250 °C, (**b**) 350 °C, (**c**) 450 °C, and BM alloy: (**d**) 250 °C, (**e**) 350 °C, (**f**) 450 °C.

Figure 7 and Table 2 show the tensile test results of the two alloys at different temperatures. As the temperature increased, the strength of the two alloys decreased, accompanied by an increase in elongation. The tensile strengths of BL alloys were 185, 46, and 18 MPa at 250, 350, and 450 °C, respectively, and the tensile strengths of BM alloys at the corresponding temperatures reached up to 205, 68, and 25 MPa, respectively. As the temperature increased, its elongation gradually increased except at 250 °C (elongation did not change between 25 and 250 °C), according to the grain refinement strengthening mechanism and precipitation strengthening mechanism in the metal strengthening. The grain refinement strengthening mechanism indicates that the finer the grain is, the higher the elongation is when other factors remain unchanged. Precipitation strengthening mechanism shows that the smaller the precipitation phase is, the more obvious the pinning effect on dislocations is. The stronger the distortion field caused by the formation of dislocation entanglement, the more difficult it is to stagger the movement, and the more difficult it is to deform, thereby leading to a reduction in plasticity. As the temperature increases, the growth trend of the precipitation phase is more obvious. It was obvious at 350 and 450 °C, bit not at 250 °C. The precipitation phase coarsened, and the number per unit volume decreased. The pinning effect was weakened, dislocations were prone to slip deformation, and plasticity was improved, which means that the elongation was increased. The grains did not change significantly from room temperature to 250 °C, as shown in Figures 1 and 4. Precipitates at 250 °C did not significantly coarsen, as shown in Figure 6. The above results indicate that, as the oxygen content increased from 0.15% to 0.33%, the tensile strength of the powder metallurgy Al-Zn-Mg-Cu alloy at various temperatures increased significantly. The elongation of the BL alloy was higher than that of BM alloy at room temperature, and this phenomenon is also reflected in dispersion-strengthened copper and steel. The difference in room temperature stretching is that the elongation of the BM alloy at 250, 350, and 450 °C significantly increased compared to that of the BL alloy. The grain size of the BM alloy was thus much smaller than that of BL alloy. Compared with BL alloys, the high performance of BM alloys can be attributed to the fact that more γ-Al_2O_3 particles hinder the movement of dislocations and limit the growth of grains.
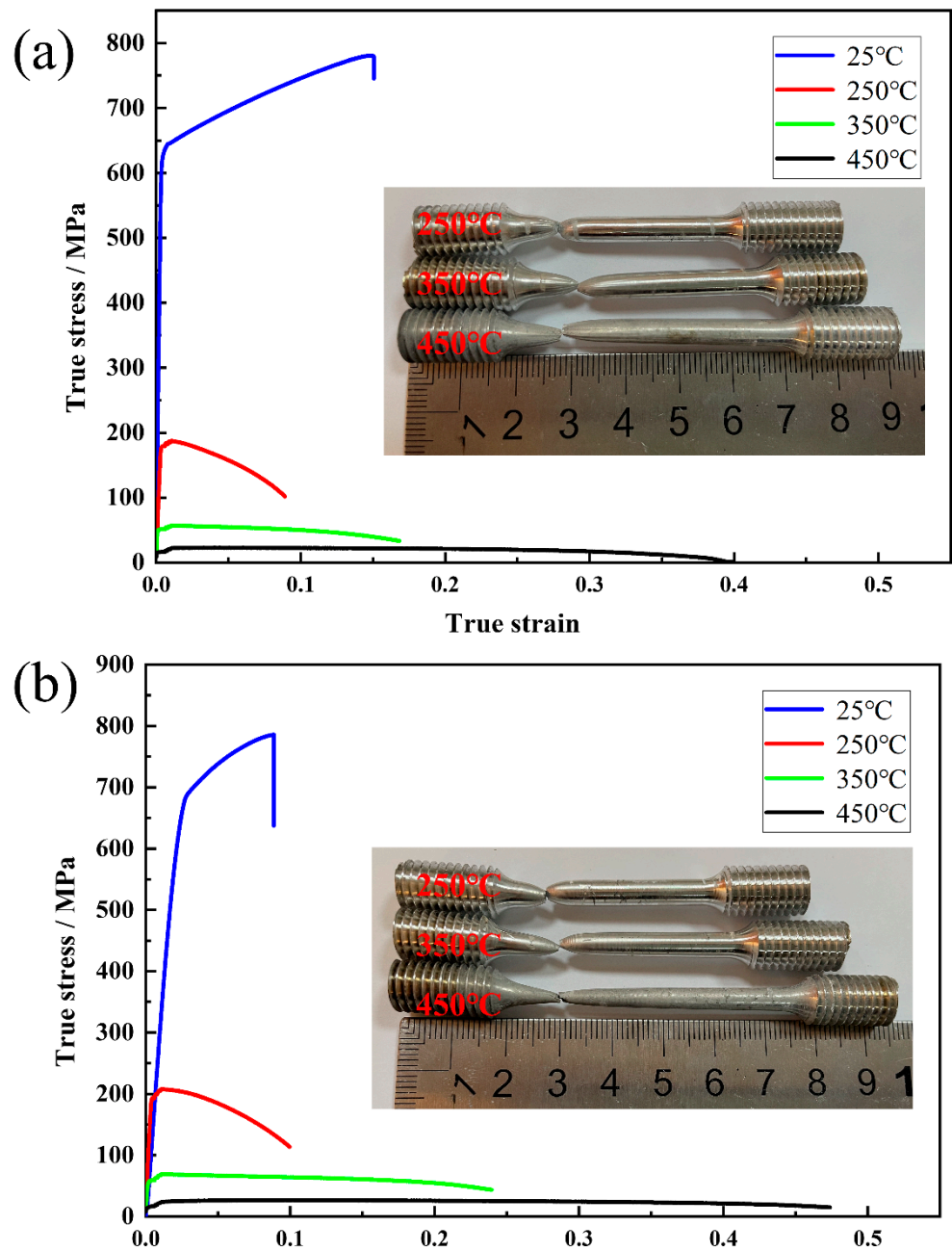
Figure 7. True strain vs. true stress curves of (**a**) BL alloy and (**b**) BM alloy.

Table 2. Mechanical properties of BL and BM alloys at different temperatures.

Sample	Temperature(°C)	UTS (Mpa)	YS (Mpa)	Elongation (%)
BL	25	677 ± 5	617 ± 5	14 ± 0.5
	250	185 ± 5	178 ± 5	13 ± 1
	350	46 ± 3	35 ± 3	33 ± 3
	450	18 ± 3	9 ± 3	45 ± 5
BM	25	716 ± 5	670 ± 5	11.5 ± 0.5
	250	231 ± 5	216 ± 5	15 ± 1
	350	68 ± 3	58 ± 3	40 ± 3
	450	25 ± 3	15 ± 3	71 ± 5

Figure 8 shows the macroscopic morphology of the tensile fractures of the two alloys at different temperatures. The necking of the two alloys was quite obvious in the high

-emperature tensile state. As temperature increased, the fracture surface was gradually rough, and the steps near the fracture were gradually obvious. Figure 9 shows the high-magnification morphology of the tensile fracture at different temperatures. The fracture surface was composed of microporous aggregate fracture platform, which signifies the character of ductile fracture. At room temperature, the two alloys had typical ductile fractures, and the dimples were quite small. As shown in Figure 9b,f, the fracture surface of the two alloys was covered with a large number of equiaxial dimples and tearing edges at the deformation temperature of 250 °C. The dimple sizes were quite small, and the coalescence of dimples could rarely be observed. This is because the deformation tended to generate some microscopic dimples rather than enlarge the previously induced small ones at relatively low deformation temperature. With the increase in deformation temperature, the coalescence of dimples is most likely to occur. Therefore, many large dimples and cracks could be observed on the fracture surface at 350 °C, as shown in Figure 9c,g. From Figure 9b,c,f,g, it can be concluded that the nucleation, growth, and coalescence of microvoids deteriorated the deformation properties of the materials and resulted in the final fracture of specimens. The main fracture mechanism was microvoid coalescence at the deformation temperatures of 250 and 350 °C. When the deformation temperature was increased to 450 °C, it was obvious that the density of dimples and tearing edges decreased, and some large voids appeared on the fracture surface in both two alloys (Figure 9d,h). Due to the high temperature, the main deformation mechanism changed from the dislocation movement to the grain boundary sliding (GBS) in the following deformation process. As a result, the deformation was concentrated at the grain boundaries, and the growth and coalescence of microvoids are impeded. No tearing edges or dimples could be observed, while many grains, voids, and cracks appeared, showing typical intergranular fracture morphology. Due to the decohesion among grains at relatively high temperature, these phenomena mainly result from the occurrence of GBS and viscous glide [29,30].
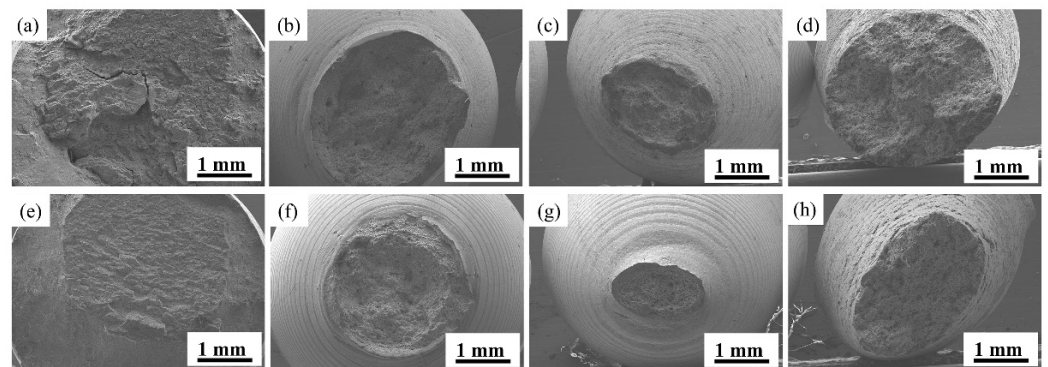

Figure 8. Macro fracture morphology of BL alloy at (**a**) 25 °C, (**b**) 250 °C, (**c**) 350 °C, (**d**) 450 °C and BM alloy at (**e**) 25 °C, (**f**) 250 °C, (**g**) 350 °C, (**h**) 450 °C.
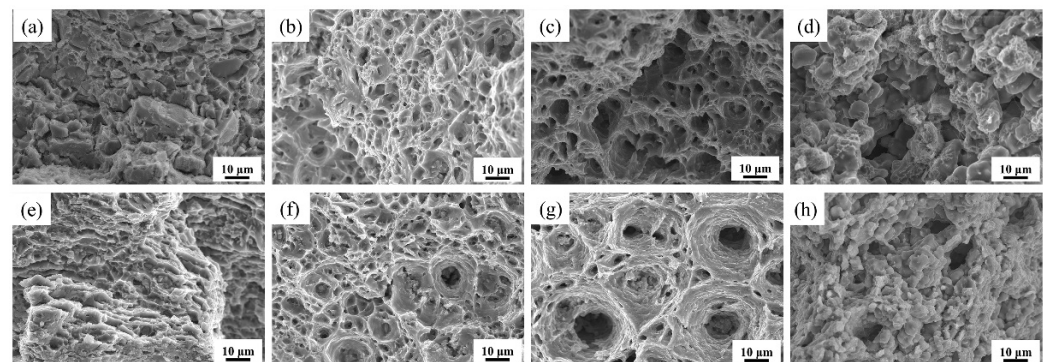

Figure 9. Micro fracture morphology of BL alloy with high magnification at (**a**) 25 °C, (**b**) 250 °C, (**c**) 350 °C, (**d**) 450 °C and BM alloy at (**e**) 25 °C, (**f**) 250 °C, (**g**) 350 °C, (**h**) 450 °C.

4. Conclusions

In this work, Al-Zn-Mg-Cu powders containing 0.15 and 0.33 wt % oxygen were utilized to prepare high-strength aluminum alloys through the process of cold isostatic pressing, sintering, hot extrusion and heat treatment. Microstructural and mechanical properties at elevated temperatures of 250, 350, and 450 °C were investigated by scanning electron microscope (SEM), electron backscatter diffraction (EBSD), transmission electron microscopy (TEM), and high-temperature tensile tests. The following conclusions were drawn:

(1) The grain sizes of the two Al-Zn-Mg-Cu alloys with oxygen content of 0.15% (BL alloy) and 0.33% (BL alloy) were 5.15 and 3.16 μm, respectively. The pinning effect of γ-Al_2O_3 particles on the movement of dislocations and grain boundaries was observed by TEM.γ-Al_2O_3 inhibits the recrystallization process of Al alloy during hot deformation processing and subsequent heat treatment through the pinning effect on dislocations and grain boundaries.

(2) The two alloys showed grain growth at 250, 350, and 450 °C. However, due to the pinning effect of γ-Al_2O_3 on the grain boundaries, the grain growth of BM alloy was not obvious. This was due to the greater amount of pinning in grain boundaries provided by more γ-Al_2O_3 in BM alloy.

(3) The tensile strengths of BL alloys were 185, 46, and 18 MPa at 250, 350, and 450 °C, respectively, while those of BM alloys were 205, 68, and 25 MPa, respectively. The UTS of the BM alloy was higher than that of the BL alloy. This might be attributed to small grain size and finer second phase in the BM alloy.

(4) The main deformation mechanism is dislocation movement at 250 and 350 °C, while grain boundary sliding occurred at 450 °C.

Author Contributions: W.H.: Conducted the literature review, conducted experiments, performed the data analyses and wrote the manuscript. Y.L.: Helped perform the analysis with constructive discussions. P.L.: Helped perform the analysis with constructive discussions. G.S.: Helped perform the analysis with constructive discussions. C.Z.: Helped perform the analysis with constructive discussions. C.S.: Helped perform the analysis with constructive discussions. C.C.: Help design the research plan, analyze the data and revise the manuscript. F.Y.: Help design the research plan, analyze the data and revise the manuscript. Z.G.: Provided the conception of this study and helped conduct the experiment. All authors have read and agreed to the published version of the manuscript.

Institutional Review Board Statement: Not applicable.

Informed Consent Statement: Not applicable.

Data Availability Statement: The data presented in this study are available on request from the corresponding author.

Conflicts of Interest: The authors declare no conflict of interest.

References

1. Liu, J.; Cheng, Y.S.; Chan, S.; Sung, D. Microstructure and mechanical properties of 7075 aluminum alloy during complex thixoextrusion. *Trans. Nonferrous Met. Soc. China* **2020**, *30*, 3173–3182. [CrossRef]

2. Moon, C.; Thuillier, S.; Lee, J.; Lee, M.G. Mechanical properties of solution heat treated Al-Zn-Mg-Cu (7075) alloy under different cooling conditions: Analysis with full field measurement and finite element modeling. *J. Alloys Compd.* **2021**, *856*, 158180. [CrossRef]

3. Wang, Y.; Wu, X.; Cao, L.; Tong, X.; Guo, M. Effect of ag on aging precipitation behavior and mechanical properties of aluminum alloy 7075. *Mater. Sci. Eng. A* **2020**, *804*, 140515. [CrossRef]

4. Lee, S.H.; Jung, J.G.; Baik, S.I.; Park, S.H.; Euh, K. Effects of Ti addition on the microstructure and mechanical properties of Al-Zn-Mg-Cu–Zr alloy. *Mater. Sci. Eng. A* **2020**, *801*, 140437. [CrossRef]
5. Guo, Y.; Zhang, M.; Wang, Z.; Wang, S.; Zhao, H. Effects of cold temperatures, strain rates and anisotropy on the mechanical behavior and fracture morphology of an Al-Zn-Mg-Cu alloy. *Mater. Sci. Eng. A* **2020**, *806*, 140691. [CrossRef]
6. Muhammad, A.K.; Wang, Y.W.; Muhammad, J.A.; Ghulam, Y.; Abdul, M.; Faisal, N.; Shahrukh, K.; Tahir, A.; Zhang, H. Effect of heat treatment on the precipitate behaviour, corrosion resistance and high temperature tensile properties of 7055 aluminum alloy synthesis by novel spray deposited followed by hot extrusion. *Vacuum* **2019**, *174*, 109185.
7. Sun, J.H.; Liang, J.; Wang, L.C.; Li, P.; Zhang, Y.Q.; Shan, C.Z. Development and application of aluminum alloy drill rod in deep drilling. *Procedia Eng.* **2016**, *73*, 84–90.
8. Wang, Y.C.; Cao, L.F.; Wu, X.D.; Huang, G.J. Research progress on microstructure and properties of 7xxx series aluminum alloys for oil drill pipes. *Mater. Rev.* **2019**, *33*, 1190–1197.
9. Easton, M.A.; Qian, M.; Prasad, A.; StJohn, D.H. Recent advances in grain refinement of light metals and alloys. *Curr. Opin. Solid State Mater. Sci.* **2016**, *20*, 13–24. [CrossRef]
10. Zhao, J.G.; Liu, Z.Y.; Bai, S.; Huang, T.T.; Wang, J.; Xie, H.Y. Effect of various aging treatment on thermal stability of a novel Al-Zn-Mg-Cu alloy for oil drilling. *Mater. Sci. Eng. A* **2021**, *803*, 140490. [CrossRef]
11. Ortiz, D.; Brown, J.; Abdelshehid, M.; Deleon, P.; Dalton, R.; Mendez, L. The effects of prolonged thermal exposure on the mechanical properties and fracture toughness of c458 aluminum–lithium alloy. *Eng. Fail. Anal.* **2006**, *13*, 170–180. [CrossRef]
12. Lee, E.W.; Oppenheim, T.; Robinson, K.; Aridkahari, B.; Neylan, N.; Gebreyesus, D. The effect of thermal exposure on the electrical conductivity and static mechanical behavior of several age hardenable aluminum alloys. *Eng. Fail Anal.* **2007**, *149*, 1538–1549. [CrossRef]
13. Chen, K.; Tang, J.; Jiang, F.; Teng, J.; Zhang, H. The role of various Zr additions in static softening behavior of Al-Zn-Mg-Cu alloys during interval holding of double-stage hot deformation. *J. Alloys Compd.* **2019**, *792*, 1112–1121. [CrossRef]
14. Zhou, M.; Lin, Y.C.; Jiao, D.; Jiang, Y.Q. Hot tensile deformation behaviors and constitutive model of an Al-Zn-Mg-Cu alloy. *Mater. Des.* **2014**, *59*, 141–150. [CrossRef]
15. Zhang, Y.; Jin, S.; Trimby, P.W.; Liao, X.; Murashkin, M.Y.; Valiev, R.Z. Dynamic precipitation, segregation and strengthening of an Al-Zn-Mg-Cu alloy (aa7075) processed by high-pressure torsion. *Acta Mater.* **2018**, *162*, 19–32. [CrossRef]
16. Xu, C.L.; Huang, J.W.; Jiang, F.Q.; Jiang, Y.G. Dynamic recrystallization and precipitation behavior of a novel Sc, Zr alloyed Al-Zn-Mg-Cu alloy during hot deformation. *Mater. Charact.* **2021**, *183*, 11162. [CrossRef]
17. Ren, J.; Wang, R.; Peng, C.; Feng, Y. Multistage aging treatment influenced precipitate characteristics improve mechanical and corrosion properties in powder hot-extruded 7055 Al alloy. *Mater. Charact.* **2020**, *170*, 110683. [CrossRef]
18. Ying, T.; Gu, L.D.; Tang, X.Y.; Wang, J.Y.; Zeng, X.Q. Effect of Sc microalloying on microstructure evolution and mechanical properties of extruded Al-Zn-Mg-Cu alloys. *Mater. Sci. Eng. A* **2022**, *831*, 142197. [CrossRef]
19. Martin, A.; Vilanova, M.; Gil, E.; Sebastian, M.S.; Wang, C.Y.; Milenkovic, S. Influence of the Zr content on the processability of a high strength Al-Zn-Mg-Cu-Zr alloy by laser powder bed fusion. *Mater. Charact.* **2022**, *183*, 111650. [CrossRef]
20. Macaskill, I.A.; Hexemer, R.L.; Donaldson, I.W.; Bishop, D.P. Effects of magnesium, tin and nitrogen on the sintering response of aluminum powder. *J. Mater. Process Technol.* **2010**, *210*, 2252–2260. [CrossRef]
21. Martin, J.M.; Castro, F. Liquid phase sintering of p/m aluminium alloys: Effect of processing conditions. *J. Mater. Process Technol.* **2003**, *143*, 814–821. [CrossRef]
22. Grayson, G.N.; Schaffer, G.B.; Griffiths, J.R. Observations of oxide films on fatigue fracture surfaces of a sintered 2xxx series aluminium alloy. *Mater. Sci. Eng. A* **2007**, *454*, 99–103. [CrossRef]
23. Ccab, C.; Feng, L.D.; Wh, A.; Tl, A.; Pei, L.A.; Qc, A. Thermally stable al conductor prepared from al powder with a low oxygen content. *Mater. Sci. Eng. A* **2021**, *813*, 141174.
24. Balog, M.; Poletti, C.; Simancik, F.; Walcher, M.; Rajner, W. The effect of native Al_2O_3 skin disruption on properties of fine al powder compacts. *J. Alloys Compd.* **2011**, *509*, S235–S238. [CrossRef]
25. Nosko, M.; Stepanek, M.; Zifcak, P.; Orovcik, L.; Nagy, S.; Dvorak, T. Solid-state joining of powder metallurgy Al-Al_2O_3 nanocomposites via friction-stir welding: Effects of powder particle size on the weldability, microstructure, and mechanical property. *Mater. Sci. Eng. A* **2019**, *754*, 190–204. [CrossRef]
26. Gyza, B.; Xl, A.; Bh, A.; Ptl, A.; Yqya, B. Distributions of grains and precipitates in gradient lamellae Al-Zn-Mg-Cu alloy by ultrasonic surface rolling processing. *Mater. Sci. Eng. A* **2021**, *825*, 141911.
27. Chen, C.C.; Han, W.H.; Qi, M.; Dong, S.P.; Li, P.; Yang, F. Microstructural evolution and mechanical properties of an ultrahigh strength Al-Zn-Mg-Cu alloy via powder metallurgy and hot extrusion. *J. Cent. South Univ.* **2021**, *28*, 1195–1205. [CrossRef]
28. Ma, K.; Hu, T.; Yang, H.; Topping, T.; Yousefiani, A.; Lavernia, E.J.; Schoenung, J.M. Schoenung. Coupling of dislocations and precipitates: Impact on the mechanical behavior of ultrafine grained Al–Zn–Mg alloys. *Acta Mater.* **2016**, *103*, 153–164. [CrossRef]
29. Lin, Y.C.; Deng, J.; Jiang, Y.Q.; Wen, D.X.; Liu, G. Effects of initial d phase on hot tensile deformation behaviors and fracture characteristics of a typical Ni-based superalloy. *Mater. Sci. Eng. A* **2014**, *598*, 251–262. [CrossRef]
30. Deng, J.; Lin, Y.C.; Li, S.S.; Chen, J.; Ding, Y. Hot tensile deformation and fracture behaviors of AZ31 magnesium alloy. *Mater. Des.* **2013**, *49*, 209–219. [CrossRef]